fluids

MDPI

Article

Hydrodynamic Resistance and Stability Analysis of a Secondary Towed Body in a Two-Stage Deep-Towing System

Ke Wang [1,*], Bolin Liu [1], Qi Zhang [1], Chengyang Zhu [1] and Chuanbo Cong [2]

[1] College of New Energy Science and Engineering, China University of Petroleum-Beijing, Beijing 102249, China
[2] College of Materials Science and Engineering, China University of Petroleum-Beijing, Beijing 102249, China
* Correspondence: wang_ke@cup.edu.cn

Abstract

This study numerically investigates the hydrodynamic resistance and stability of a two-stage towing system. A coupled fluid–structure interaction model comprising a primary body, catenary cable, and secondary body is evaluated under fully constrained, linearly constrained, and planarly constrained conditions. By simulating idealized infinite-depth operations, the inter-body wake interference, drag forces, and cable tension were analyzed at varying towing distances. Results indicate that as the towing distance increases, the secondary body gradually exits the highly disturbed wake region of the primary body. Consequently, the wake field becomes symmetrical, and both the hydrodynamic drag and mean cable tension progressively increase. Despite experiencing higher drag, a larger separation distance effectively diminishes reciprocating motions and significantly enhances the overall longitudinal translational stability of the system. This comparative assessment intentionally focuses on resistance-dominated wake shielding and translational stability. Rotational dynamics including explicitly extracted lift forces and trimming moments are reserved for future unconstrained six-degree-of-freedom studies.

Keywords: two-stage towing system; hydrodynamic resistance; wake interaction; towing stability; numerical simulation

1. Introduction

Deep-sea exploration is a crucial pathway to achieving sustainable global development, with technological advancements directly driving the progress of marine science. Propelled by the growing demand for oceanographic research and the acceleration of marine equipment industries, deep-sea exploration technology is entering a period of rapid growth [1–5]. The two-stage deep-towing system is a critical component of this domain. It typically consists of a mother ship, a primary cable (armored umbilical), a primary towed body (depressor), a secondary cable (tether), and a secondary towed body. In real deep-sea operations the two-stage configuration is extensively utilized. The heavy primary body serves fundamentally as a massive heave decoupler. It is intentionally designed to absorb the severe high-frequency heave and pitch motions transmitted from the mother ship via the main tow cable. This mechanism effectively isolates disturbances and creates a relatively stable towing environment for the neutrally buoyant secondary body carrying sensitive acoustic and optical instruments. This system has extensive applications in marine engineering and scientific research, including marine environmental monitoring, geological surveys, and seabed mapping [4,5].

In practical two-stage deep-towing operations, the secondary body usually works as a measurement or observation platform behind the primary depressor, as depicted in Figure 1.

Check for updates

Academic Editors: Xavier Carton, Bingfu Zhang, Hui Tang, Mingming Zhang and Xiaowei Deng

Received: 27 August 2026
Revised: 19 October 2026
Accepted: 5 November 2026
Published: 13 November 2026

Copyright: © 2026 by the authors. Licensee MDPI, Basel, Switzerland. This article is an open access article distributed under the terms and conditions of the Creative Commons Attribution (CC BY) license.

Its hydrodynamic environment is therefore determined not only by the incoming towing speed but also by the primary-body size, secondary-body size, separation distance, cable properties, deployment depth, and the recovery of the primary-body wake. On this basis, the present numerical model defines a representative operating condition and focuses on how the downstream wake modifies the resistance and stability of the secondary body, rather than attempting to reproduce every possible field-deployment condition.

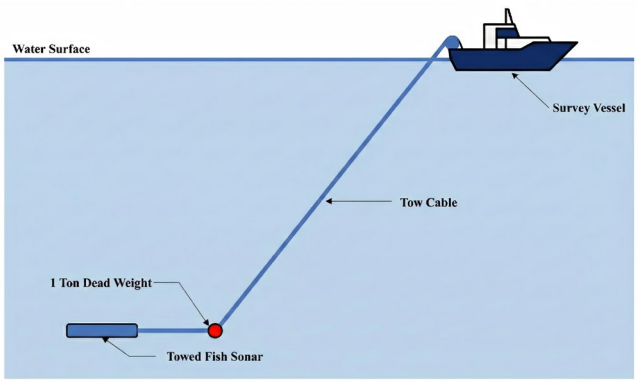

Figure 1. Two-stage underwater towed system.

Underwater towed systems experience complex hydrodynamic forces, including drag, lift, and moments, which are characterized by strong nonlinearity and multi-factor coupling due to fluid viscosity [6,7]. To understand these dynamics, researchers have utilized both experiments and numerical simulations. Experimental studies, such as those by Bettles and Chapman [8] and Mansoorzadeh and Javanmard [9], have provided valuable data on hydrodynamic derivatives and the effects of velocity on drag and lift. Theoretically, models for cable dynamics have evolved from simple steady-state analysis [10] to complex unsteady differential equations [11,12]. With the rise of CFD, researchers like Wu and Chwang [13,14] and Yang et al. [15,16] have successfully calculated added mass and analyzed system dynamics under oscillatory motions. However, most existing studies tend to treat the mother ship, cable, and towed bodies as independent entities, heavily relying on simplified decoupled models and empirical hydrodynamic coefficients. These conventional approaches inherently fail to capture the highly nonlinear fluid–structure interactions between the two stages. Specifically, there remains a critical lack of comprehensive analysis regarding how the massive turbulent wake generated by the primary bluff body dynamically interferes with the surrounding flow field and the spatial stability of the secondary towed body under different operational constraints. This specific limitation in resolving fully coupled, body-to-body wake interference directly motivates the present study.

To address these limitations, this study employs CFD methods to conduct a coupled hydrodynamic analysis of the two-stage towing system, modelling the primary towed body, the connecting cable, and the secondary towed body as an integrated system. The hydrodynamic performance is investigated under three idealized kinematic constraint cases: fully constrained, linearly constrained, and planarly constrained conditions in an infinite-depth domain. These cases are introduced as progressive boundary conditions for mechanism identification, not as exact replicas of all operational degrees of freedom encountered during field deployment. The primary objective is to elucidate the impact of towing distance on the drag characteristics, surface pressure distribution, and wake-field symmetry of the secondary towed body. Furthermore, the study analyzes the tension in the secondary cable and the flow-induced stability trend of the system. The novelty of the present work lies in establishing a coupled CFD framework for the primary body–cable–secondary body assembly and using a hierarchical constraint-release strategy to

isolate how wake shielding, cable-force redistribution, and coupled body motions jointly influence the resistance and stability of the secondary towed body. The constrained cases are therefore interpreted as comparative analysis scenarios with clear applicability limits, while a complete six-degree-of-freedom field model with realistic ship motion, cable elasticity, and environmental disturbance remains a subject for future work.

The remainder of this paper is organized as follows. Section 2 details the numerical methodology, including the governing equations of the fluid domain, the coupled rigid-body dynamics, the quasi-static elastic catenary formulation, the computational domain with overset mesh configurations, and the numerical verification studies. Section 3 presents and analyzes the hydrodynamic resistance, wake flow evolution, and dynamic stability of the two-stage towing system across three progressive constraint setups (fully constrained, linearly constrained, and planarly constrained conditions), followed by a comprehensive synthesis of the parametric trends and an evaluation of the model limitations. Finally, Section 4 summarizes the primary conclusions of this study and outlines directions for future research.

2. Numerical Methods and Computational Model

2.1. Governing Equations

The incompressible turbulent flow around the towed system is governed by the Reynolds-Averaged Navier–Stokes (RANS) equations, described as follows:

$$\frac{\partial \overline{u_i}}{\partial x_i} = 0 (i = 1, 2, 3) \tag{1}$$

$$\rho\left[\frac{\partial u_i}{\partial t} + \frac{\partial\left(\overline{u_i u_j}\right)}{\partial x_j}\right] = -\frac{\partial P}{\partial x_i} + \rho g_i + \rho \frac{\partial}{\partial x_j}\left[\nu\left(\frac{\partial \overline{u_i}}{\partial x_j} + \frac{\partial \overline{u_j}}{\partial x_i}\right) - \overline{u_i' u_j'}\right] \quad (i, j = 1, 2, 3) \tag{2}$$

where $\overline{u_i}$ and $\overline{u_j}$ are the velocity components of the fluid in i and j directions, respectively; x_i is the rectangular coordinate of space, ρ is the density of the fluid, P is the mean value of pressure, μ is the dynamic viscosity coefficient of the fluid, g_i is the mass force component, and $-\rho\overline{u_i' u_j'}$ is the Reynolds stress term.

To close the governing equations, the Realizable k-ε turbulence model was selected due to its balance of computational efficiency and accuracy in simulating underwater vehicle hydrodynamics [15–17]. More importantly, compared to standard formulations, the Realizable model demonstrates superior robustness and predictive accuracy for complex turbulent flows involving adverse pressure gradients, strong streamline curvature, and massive flow separation. Because these complex flow phenomena are highly prevalent in the near-wake region of the bluff primary body, this model is highly suitable for predicting the mean hydrodynamic loads and large-scale wake interaction characteristics within the scope of the present study. The transport equations for the turbulent kinetic energy k and the turbulent dissipation rate ε are formulated as:

$$\rho\frac{\partial k}{\partial t} + \rho\frac{\partial}{\partial x_j}\left(k\overline{u_j}\right) = \frac{\partial}{\partial x_j}\left[\left(\mu + \frac{\mu_t}{\sigma_k}\right)\frac{\partial k}{\partial x_j}\right] + G_k + G_b - \rho\varepsilon - Y_M + S_k \tag{3}$$

$$\begin{aligned}\rho\tfrac{\partial}{\partial t}(\varepsilon) \quad &+\rho\tfrac{\partial}{\partial x_j}\left(\varepsilon\overline{u_j}\right) = \tfrac{\partial}{\partial x_j}\left[\left(\mu + \tfrac{\mu_t}{\sigma_\varepsilon}\right)\tfrac{\partial \varepsilon}{\partial x_j}\right] + \rho C_1 S\varepsilon - \rho C_2 \tfrac{\varepsilon^2}{k + \sqrt{v\varepsilon}} \\ &+C_{1\varepsilon}\tfrac{\varepsilon}{k}C_{3\varepsilon}G_b + S_\varepsilon\end{aligned} \tag{4}$$

where k is the turbulent kinetic energy and ε is the dissipation rate; μ_t is the turbulent viscosity; v is the kinematic viscosity; and S is the modulus of the mean rate-of-strain tensor. The terms C_1, $C_{1\varepsilon}$, and C_2 are model constants; $C_{3\varepsilon}$ accounts for buoyancy effects; while σ_k and σ_ε are the turbulent Prandtl numbers for k and ε, respectively. Additionally, G_k

represents the generation of turbulent kinetic energy due to mean velocity gradients, G_b denotes the generation due to buoyancy, and Y_M represents the contribution of fluctuating dilatation in compressible turbulence. S_k and S_ε are user-defined source terms.

To quantitatively evaluate the fluid–structure interaction loads and the wake recovery characteristics analyzed in the subsequent sections, the total hydrodynamic drag force acting on the towed body (F_d), the characteristic Reynolds number (Re), the dimensionless inter-body separation ratio (L^*), and the normalized axial flow velocity (U_x^*) are defined, respectively, as:

$$F_d = \int_s (p_s \boldsymbol{n} + \tau_s) \cdot \boldsymbol{e}_x d\alpha_s, Re = \frac{\rho U_0 D}{\mu}, L^* = \frac{L}{D}, U_x^* = \frac{U_x}{U_0} \tag{5}$$

where p_s and $\boldsymbol{\tau}_s$ denote the normal pressure and tangential viscous shear stress acting on the body surface element $d\alpha_s$, $\mathbf{n}$ is the unit outward normal vector, $\mathbf{e}_x$ is the unit vector along the streamwise direction, U_0 is the undisturbed free-stream towing velocity, D is the characteristic diameter of the primary body, L is the relaxed cable length, and U_x is the local streamwise velocity in the wake field.

However, the use of a RANS-based Realizable k-ε model also defines an important limitation of the present study. The model is intended to capture mean resistance, mean pressure distribution, and large-scale wake interaction, but it is not designed to resolve all fine-scale coherent vortices, vortex-induced vibration, or transient trimming-moment characteristics with the same fidelity as high-resolution scale-resolving simulations.

2.2. Motion Equations of the Towing System

The underwater motion of the towed body involves complex six-degree-of-freedom (6-DOF) coupling, influenced simultaneously by the cable tension, hydrodynamic forces, gravity, and buoyancy.

In the subsequent numerical cases, selected degrees of freedom are deliberately restricted to isolate individual physical mechanisms. Thus, the fully constrained, linearly constrained, and planarly constrained cases should be regarded as idealized boundary cases for comparative analysis rather than as a complete representation of the real sea-state motion of the two-stage system.

2.2.1. Rigid Body Dynamics

The Dynamic Fluid–Body Interaction (DFBI) module in STAR-CCM+ 2206 (Siemens Digital Industries Software, Plano, TX, USA) is employed to simulate the rigid body motion. The module integrates fluid pressure and shear forces acting on the body surface with external forces (e.g., gravity and cable tension) to solve the governing equations of motion. While the module calculates the full 6-DOF response (surge, sway, heave, roll, pitch, and yaw), this study primarily analyzes the surge and heave motions to evaluate depth-keeping performance and stability. The equations of motion for the towed body in the body-fixed coordinate system are given by Yang et al. [15,16]:

$$m\frac{du}{dt} = \sum_s p_s \alpha_s - \sum_s \tau_s \alpha_s + mg + F_t \tag{6}$$

$$M\frac{d\omega}{dt} + \omega \times M\omega = \sum_s [r_s \times (p_s \alpha_s)] - \sum_s [r_s \times (\tau_s \alpha_s)] + r_t \times F_t \tag{7}$$

where m is the mass of the towed body; u and ω are the linear and angular velocities of the traveling towing body, respectively; α_s is the area of the surface element of the towed body surface; p_s and τ_s are the normal and shear forces acting on the surface element s by the fluid, respectively; F_t is the towing force exerted by the towing cable on the towing body; r_t

and r_s are the distance vectors of s and the point of the cable to the center of gravity of the towing body; and M is the mass inertia of the rotation:

$$M = \begin{bmatrix} M_{xx} & M_{xy} & M_{xz} \\ M_{xy} & M_{yy} & M_{yz} \\ M_{xz} & M_{yz} & M_{zz} \end{bmatrix} \tag{8}$$

2.2.2. Cable Dynamics

In this study, the hydrodynamic forces acting directly on the thin inter-body cable are neglected. This assumption is justified by the scale of the specific problem investigated: because the study focuses on intense body-to-body turbulent wake interference at relatively short separation distances (up to 15 m), the massive hydrodynamic loads acting on the large bluff bodies strongly dominate the coupled dynamics of the system. While cable drag is a crucial factor for kilometers-long primary tow cables, it plays a secondary role at these short inter-body scales. Moreover, consistent with established modeling strategies for two-part towed systems [15,17], treating the short tether as a quasi-static elastic catenary effectively captures the crucial mechanical coupling, tension variations, and stiffness effects induced by the relative motions of towed bodies, while preserving computational feasibility for the 3D fluid domain. The schematic of the cable forces and coordinates is illustrated in Figure 2. The shape equations are expressed as follows [18]:

$$\begin{cases} x = a\lambda + bsinh(\lambda) + \alpha \\ y = acosh(\lambda) + \frac{b}{2}sinh^2(\lambda) + \beta \end{cases}$$

$$a = \frac{c}{m_o g}, b = \frac{ca}{kL_r}, c = \frac{m_o g L_r}{\sinh(\lambda_2) - \sinh(\lambda_1)}, \lambda_1 \le \lambda \le \lambda_2 \tag{9}$$

where m_o is the mass per unit length of the tow cable, k is the stiffness of the tow cable, L_r is the length of the tow cable in the relaxed state, α, β are integration constants, and the curve parameter λ is related to the tangential angle φ at the point on the tow cable. It should be noted that while classical catenary formulations often define a touchdown point (TDP) for seabed mooring applications, the inter-body cable in the present mid-water towing system is fully suspended between the attachment point on the primary body P_1 and the attachment point on the secondary body P_2 without seabed contact. Within this suspended configuration, the reference vertex of the catenary curve mathematically represents the local sag minimum along the suspended span rather than a physical seabed boundary.

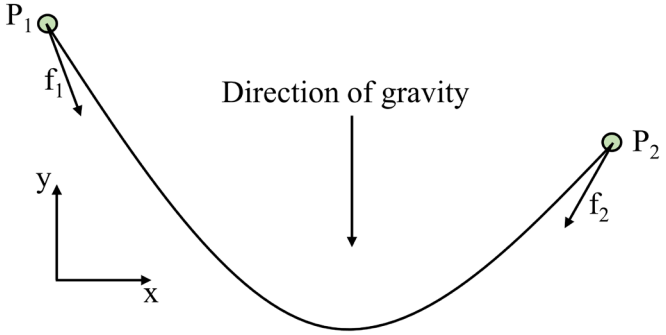

Figure 2. Cable mechanics and coordinate system.

2.3. Physical Model and Computational Domain

2.3.1. Geometric Model

The two-stage towing system analyzed in this study comprises a primary towed body (acting as a depressor), a secondary towed body, and connecting cables. Figure 3 presents the geometric model of the two-part towed system used in the simulation. The primary towed body was deliberately simplified as a vertical cylinder because it acts as a canonical bluff body. This simplification adheres to the principle of preserving essential physics while minimizing geometric interference. It ensures the generation of a strong and well defined turbulent wake while preventing complex geometric details from obscuring the fundamental body-to-body interference mechanisms. This simplification allows the influence of towing distance and constraint release to be examined more clearly, whereas a fully detailed depressor geometry will be considered in future engineering-specific studies. The influence of the mother ship is not considered in this specific simulation setup. The detailed geometric and mass parameters for the primary and secondary towed bodies are listed in Tables 1 and 2, respectively.

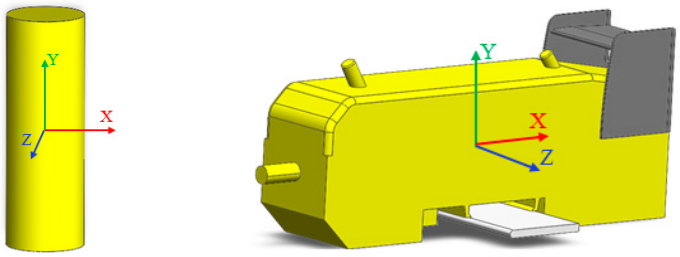

Figure 3. Primary and secondary towed bodies.

Table 1. Dead weight parameters.

Dead Weight	Value
Mass in air (kg)	1000
Diameter (m)	0.4
Length (m)	1.2
Volume (m^3)	0.15

Table 2. Towed body parameters.

Towed Body		Value
Mass in air (kg)		3290.25
Total length (m)		3.8
Volume (m^3)		3.21
Center of gravity (m)	x	0.42
	y	−0.06
	z	1.01

2.3.2. Catenary Model

The cables connect the adjacent bodies. As depicted in Figure 4, the cables are attached to the stern of the leading body and the bow of the trailing body, initially set to a slack state. The specific parameters of the towing cables are provided in Table 3.



Figure 4. Schematic of the catenary connection model between the towed bodies.

Table 3. Catenary parameters.

Parameters	Value
Relaxation length (m)	5, 10, 15
Mass per unit length (kg/m)	0.57
Stiffness (N/m)	10,000

Based on the characteristic diameter of the primary body ($D = 0.4$ m), the selected relaxed cable lengths of 5, 10, and 15 m correspond to dimensionless separation distances of $L/D = 12.5$, 25, and 37.5, respectively. The physical basis for selecting these specific distances relies on the typical wake-decay length scales for bluff cylinders operating at Reynolds numbers in the order of 10^5~10^6 (corresponding to the 3.0-knot speed). These dimensionless spacings mathematically ensure that the secondary body traverses three distinct regimes: a strong near-wake interaction region (L/D near 10), an active transitional wake-recovery region (L/D around 25), and a weakened far-wake interference region (L/D approaching 40). These distances are not intended to define universal spacing values. In general, the effective interaction distance should scale with the characteristic dimensions of the primary and secondary bodies, Reynolds number, towing velocity, turbulence intensity, and wake-decay length. Therefore, when the body size or towing speed changes, the spacing at which the secondary body approaches an undisturbed-flow response may also change.

2.3.3. Computational Domain and Boundary Conditions

To faithfully replicate the hydrodynamic behavior of the towing system during deep-sea operations, the simulation is conducted in a pseudo-infinite fluid domain. Because the objective is to examine body–body hydrodynamic interference in deep water, the computational setup neglects the free surface and bottom boundary and therefore represents an idealized infinite-depth environment. A composite domain strategy utilizing Overset Meshes (Chimera Grid) was adopted to accommodate the large-amplitude relative motions between the primary and secondary towed bodies. As illustrated in Figure 5, the computational domain is decomposed into three distinct functional regions:

a. Stationary Background Region (Subdomain I): A large rectangular prism with dimensions L × B × D = 35 m × 12 m × 20 m. To eliminate boundary interference and ensure the blockage effect is negligible, sufficiently large clearance zones were established. Specifically, the inlet is positioned 5 m upstream of the primary towed body to guarantee a uniform incoming flow, while the outlet is extended downstream to fully capture the far-field wake development and prevent reverse flow at the boundary.
b. Overset Component Regions (Subdomains II and III): Subdomain II (Cylindrical: $R = 0.6$ m}, $H = 2$ m) and Subdomain III (Rectangular: 5 m × 3 m × 3 m) encapsulate the primary and secondary towed bodies, respectively. These regions move synchronously with the rigid bodies within the background mesh, facilitating the calculation of 6-DOF motions.

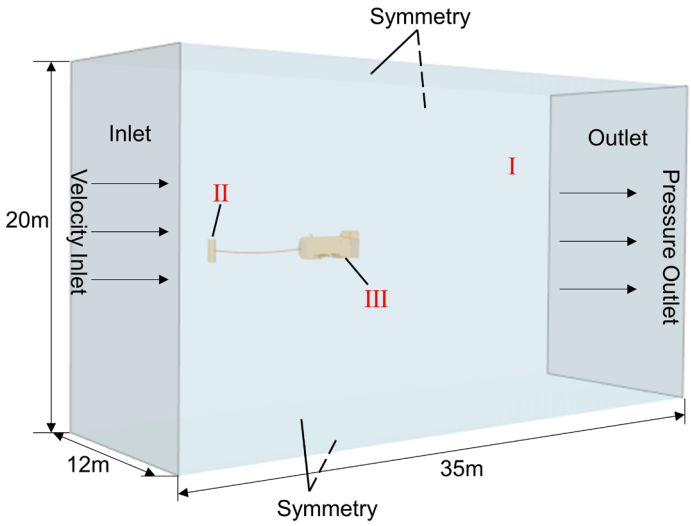

Figure 5. Computational domain and boundary conditions for the numerical simulation.

Based on the principle of relative motion the towing operation is simulated by imposing a uniform inflow velocity of 1.543 m/s at the inlet. This specific velocity is exactly equivalent to 3.0 knots. It represents the standard and most typical operational cruising speed for deep sea towing surveys worldwide. This reference operating condition is used throughout the comparative simulations so that the influence of towing distance and constraint release can be evaluated without introducing an additional velocity variable. Regarding the boundary conditions, the upstream boundary of the background domain is defined as a velocity inlet, while the downstream boundary is set as a pressure outlet with zero gauge pressure. The lateral boundaries are set as symmetry planes to approximate an unbounded ocean environment [17]. The interfaces between the component regions and the background region are defined as overset mesh interfaces to ensure conservative interpolation of flow variables. Finally, the surfaces of both the primary and secondary towed bodies are treated as no-slip walls to accurately resolve the viscous boundary layer. It should be emphasized that different towing velocities, body depths, and water depths may change the absolute resistance levels; these effects are outside the scope of the present parametric study and will be examined in subsequent work.

2.4. Meshing

The discretization of the computational domain is a critical factor influencing numerical accuracy and stability. As illustrated in Figure 6, a hybrid meshing strategy was adopted in this study to balance computational efficiency with geometric fidelity.

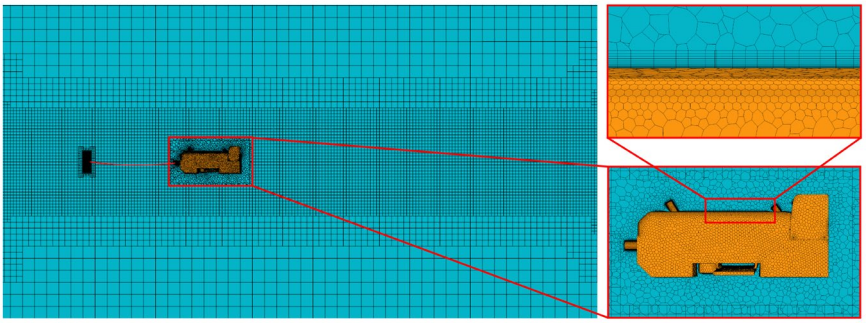

Figure 6. Computational mesh distribution showing the domain discretization and local refinement details around the towed bodies.

Specifically, Subdomains I and II were discretized using trimmed cell meshes. This approach efficiently handles the large background volume and the relatively simple geometry of the primary cylinder [19]. In contrast, Subdomain III employed Polyhedral meshes. Polyhedral cells are superior when it comes to resolving complex flow gradients and minimizing numerical diffusion, making them ideal for capturing the detailed flow physics around the secondary towed body [20,21].

To ensure accurate computation of the boundary layer and near-wall turbulence, prism layer meshes were generated on the surfaces of both towed bodies. The first layer thickness was determined based on the requirements of the high-Reynolds number k-ε turbulence model, targeting a dimensionless wall distance of $y^+ \approx 30$. Accordingly, 14 prism layers were generated with a stretching ratio of 1.2 to ensure a smooth transition from the viscous sublayer to the core mesh. Figure 6 provides a detailed view of the mesh distribution and the local refinement in the wake regions.

2.5. Verification and Sensitivity Analysis

2.5.1. CFD Method Validation

To validate the reliability of the proposed CFD framework, the standard DARPA SUBOFF model [22] was employed as a benchmark. The objective was to assess the accuracy of the numerical solver in predicting the hydrodynamic total resistance.

The validation simulation replicated the conditions of the towing tank tests. The computational setup utilized the same domain strategy, mesh topology, and turbulence model as the primary study. A total of approximately 2.99 million computational cells were generated. The geometric model and the corresponding fluid domain for the validation are presented in Figure 7. Key parameters, including the hull geometry and inlet velocity, were kept strictly consistent with the experimental setup.

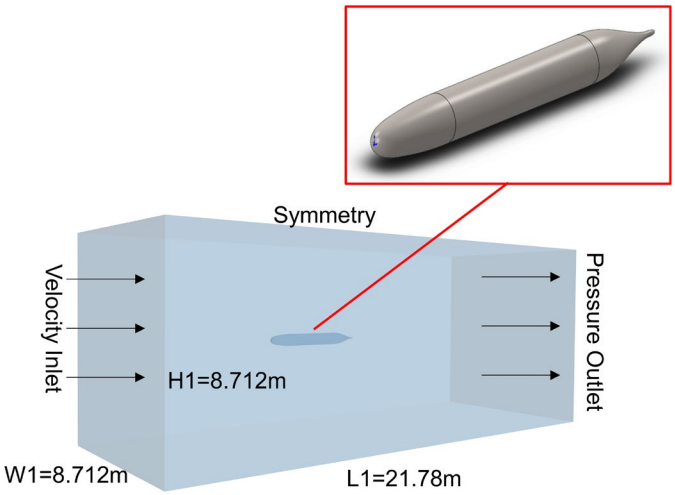

Figure 7. Geometric model and fluid computational domain configuration used for the DARPA SUBOFF validation study.

The comparison between the numerical results and the experimental data is summarized in Figure 8. The absolute error in total resistance ranges from 0.2% to 4.42% across different velocities. This strong correlation confirms that the numerical method possesses high fidelity and is suitable for the hydrodynamic analysis of the towed system. This validation against an established benchmark provides the quantitative baseline needed to support the credibility of the subsequent comparative analyses for the towing system. However, it must be acknowledged that while the SUBOFF benchmark effectively validates the CFD solver for single-body resistance, it cannot fully replicate the complex mutual wake

interference inherent in a two-body system. Future dedicated experimental model tests for the specific two-stage towing configuration are necessary to further validate the coupled hydrodynamic responses.

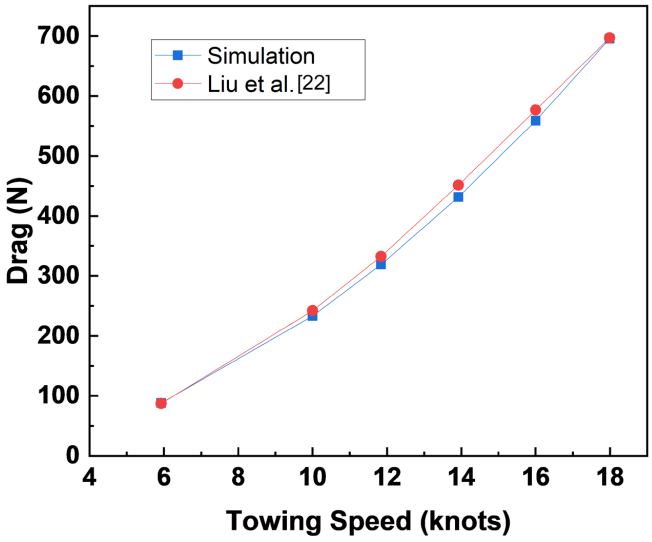

Figure 8. Comparison of CFD predictions and experimental data for SUBOFF model resistance.

2.5.2. Mesh Sensitivity Analysis

To evaluate the influence of discretization density on the results, a mesh independence study was conducted. Three mesh schemes with varying element counts were generated: coarse ($N_1 = 565{,}440$), medium ($N_2 = 1{,}222{,}698$), and fine ($N_3 = 2{,}917{,}064$). The drag force on the primary towed body was monitored as the convergence indicator. The drag force of the primary body was utilized as the baseline convergence metric because the massive flow separation originating from this upstream bluff body constitutes the physical source of the downstream interference; resolving this accurately is a strict prerequisite for generating a reliable wake field. Additionally, further verification confirmed that the drag force acting on the secondary body simultaneously satisfies the grid independence criteria under the selected N_2 mesh scheme.

Figure 9 presents the results of the mesh independence verification, with errors reported relative to the fine mesh N_3. The results indicate that the medium mesh scheme N_2 offers a balanced compromise between computational efficiency and accuracy, with the drag deviation being within an acceptable range. Consequently, the N_2 mesh scheme was adopted for the final analysis.

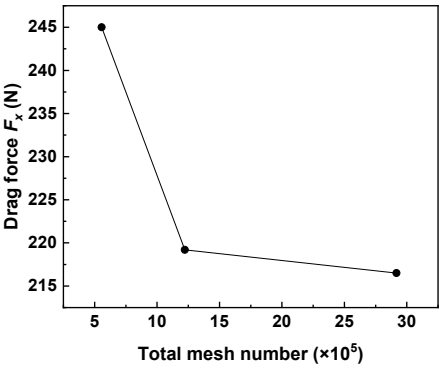

Figure 9. Variation in the drag force of the primary body with different grid densities during the mesh independence verification.

2.5.3. Time-Step Sensitivity Analysis

Temporal discretization errors were investigated by testing three different time steps: Δt = 0.001 s, 0.005 s, and 0.01 s. All other configurations remained identical to the N_2 mesh setup. The resulting converged drag forces corresponding to the three selected time-step values are shown in Figure 10. The data indicate that the computational results are highly consistent across the three time steps, demonstrating that the solution is insensitive to the time step within this range. Considering the trade-off between temporal resolution and computational cost, a time step of 0.005 s was selected for the final analysis. To provide an explicit quantitative comparison complementing Figures 9 and 10, the specific discretization parameters, converged drag forces, and relative deviations with respect to the finest resolution benchmarks (N3 and Δt = 0.001 s) are summarized in Table 4.

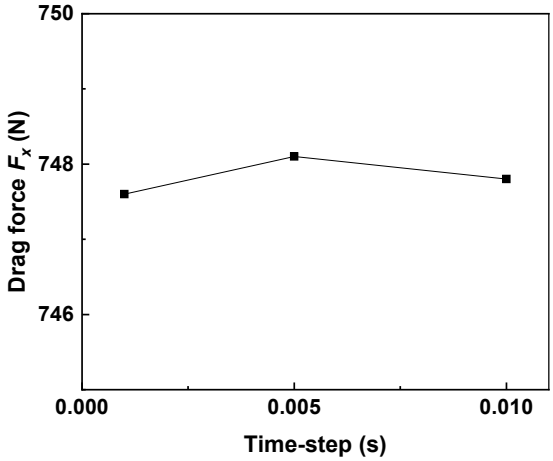

Figure 10. Variation in the drag force calculated under three different time-step values for the time-step sensitivity analysis.

Table 4. Quantitative summary of the mesh independence and time-step sensitivity analyses.

Verification Type	Scheme/ Parameter	Discretization Value	Primary Body Drag (N)	Relative Deviation (%)
Mesh Independence (Δt = 0.005 s)	N_1	565,440 cells	245.0	13.2%
	N_2	1,222,698 cells	219.2	1.22%
	N_3	2,917,064 cells	216.5	—
Time-Step Sensitivity (Mesh N_2)	Δt_1	0.010 s	747.80	0.027%
	Δt_2	0.005 s	748.10	0.067%
	Δt_3	0.001 s	747.60	—

3. Results and Discussion

To accurately simulate the behavior of the two-stage towed system in real deep-sea environments, the system should ideally be modeled with full six degrees of freedom to capture the unconstrained motion of each rigid body. However, the complex turbulent interaction and high-frequency oscillations under unconstrained conditions often lead to irregular trajectories and convergence difficulties, thereby significantly increasing computational costs. To balance computational efficiency with physical fidelity, this study evaluates the hydrodynamic performance under three progressive constraint conditions. These conditions include fully constrained, linearly constrained, and planarly constrained setups. It is crucial to emphasize that these configurations are idealized boundary cases designed strictly for mechanism identification, rather than exact engineering replicas of real

sea-state operations. They do not fully represent the unconstrained six-degree-of-freedom motions encountered in real-world deep-towing scenarios. By systematically releasing specific degrees of freedom, we can isolate the coupling effects among the cable tension, hydrodynamic loads, and spatial motions. Throughout these distinct scenarios, the towing separation distance is selected as the primary independent control variable because it most directly dictates the intensity of the wake interference, allowing the extraction of the fundamental wake shielding and momentum recovery mechanisms.

3.1. Fully Constrained Conditions

Under fully constrained conditions, all degrees of freedom of the towing system are restricted. The primary and secondary towed bodies are fixed relative to each other on the same horizontal plane, and the connecting cable is modeled as a rigid link. The system is treated as stationary in the computational domain, with hydrodynamic forces generated solely by the incoming flow. This idealized steady-state simulation serves as a baseline for analyzing the pure wake interaction effects without the complexity of spatial motion. This section analyzes the dimensionless velocity fields, drag characteristics, and surface pressure distributions at three distinct towing separation distances of 5 m, 10 m, and 15 m. Although this condition is idealized, it is useful for extracting the baseline wake-shielding effect before additional motion-induced coupling is introduced.

Figure 11 illustrates the dimensionless axial velocity contours on the horizontal plane U_x/U_0 for the fully constrained towing system. The sub-figures correspond to separation distances of 5 m, 10 m, and 15 m. As observed in the contours, a distinct velocity deficit region is generated behind the primary towed body due to flow separation and viscous dissipation. At a short distance of 5 m ($L/D = 12.5$), the secondary towed body is deeply immersed in the near-wake of the primary body. The incoming flow encountering the bow of the secondary body possesses low momentum, creating an extensive low-velocity zone between the two bodies and a large recirculation region surrounding the stern. As the separation increases to 10 m and 15 m, the flow velocity in the inter-body region rises because the wake generated by the primary body undergoes momentum recovery through continuous mixing with the surrounding free stream. Consequently, the low-speed region at the bow decreases leading to a steeper velocity gradient and a thinner boundary layer around the secondary body. The low-velocity zone at the stern also diminishes accordingly.

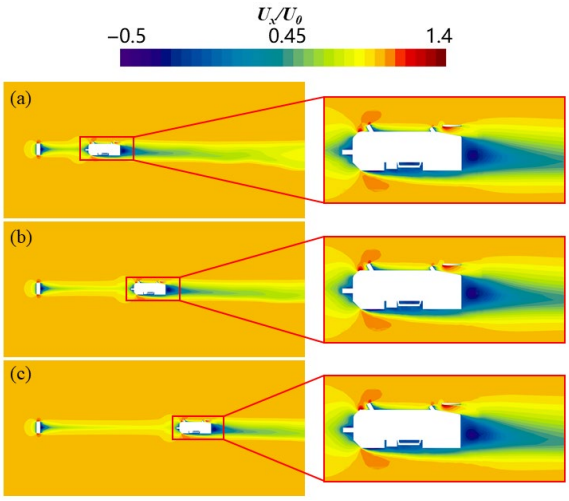

Figure 11. Dimensionless axial velocity contours on the horizontal plane for the fully constrained towing system at separation distances of (**a**) 5 m, (**b**) 10 m, and (**c**) 15 m.

Further analysis was conducted on the vertical symmetry plane as shown in Figure 12. To quantify the wake evolution, velocity profiles were extracted at five specific vertical cross-sections, as presented in Figure 13. The profiles reveal that the wake structure of the towing system is approximately symmetrical. A longitudinal comparison of the profiles near the stern of the secondary body indicates that the flow field behind the secondary towed body becomes progressively more symmetrical and stable as the towing distance increases. This suggests that increasing the separation distance allows the turbulent structures shed by the primary body to dissipate, thereby reducing the wake-induced disturbance on the secondary body.

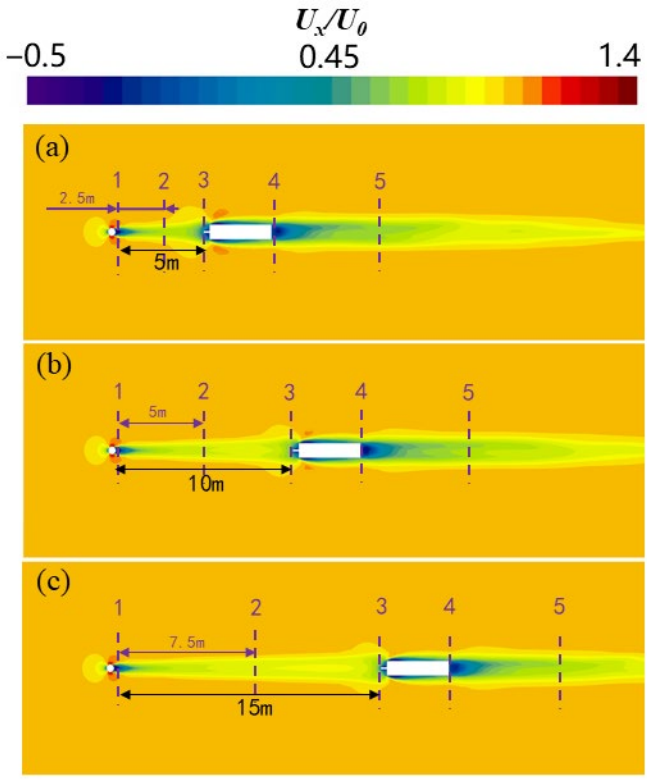

Figure 12. Dimensionless axial velocity distribution on the vertical symmetry plane for the fully constrained towing system at separation distances of (**a**) 5 m, (**b**) 10 m, and (**c**) 15 m.

Figure 14 depicts the hydrodynamic drag force of the secondary towed body at different separation distances under fully constrained conditions. The results demonstrate a clear trend where the drag force gradually increases as the separation distance increases. This phenomenon is fundamentally governed by the wake shielding effect. When the secondary body is located at a close distance, it resides within the wake shadow of the primary body, where the local inflow velocity is significantly lower than the free-stream velocity. Since hydrodynamic drag is proportional to the square of the local velocity, the drag force is considerably reduced. As the distance increases, the wake of the primary body dissipates, and the local flow velocity recovers towards the free-stream value. Consequently, the shielding effect diminishes, resulting in a progressively higher drag value. From an analytical perspective, this behavior is governed by the nonlinear momentum recovery of a turbulent bluff-body wake, where the centerline velocity deficit decays inversely with the fractional power of the downstream distance. As shown by the quantitative velocity profiles at Plane 2 in Figure 13, the centerline axial velocity ratio (U_x/U_0 at $Z = 0$) in the inter-body region recovers substantially from approximately 0.65 at 5 m to 0.78 at 10 m, whereas it increases more gradually to approximately 0.85 at 15 m. Because hydrodynamic drag is proportional to the square of the local inflow velocity, this decelerating rate of

velocity recovery directly accounts for the reduced drag increment between 10 m and 15 m. However, because U_x/U_0 at 15 m still remains below the undisturbed free-stream value of 1.0 and only three separation distances were evaluated, a unique critical threshold distance cannot be rigorously determined. The present results only indicate a gradual recovery trend toward a less-disturbed flow regime for the investigated geometry and towing speed, while determining the exact spacing required to fully reach the isolated-body drag level requires additional simulations across a wider range of separation distances. The corresponding threshold distance should depend on the primary-body characteristic length, wake-decay rate, towing speed, turbulence intensity, and secondary-body geometry.

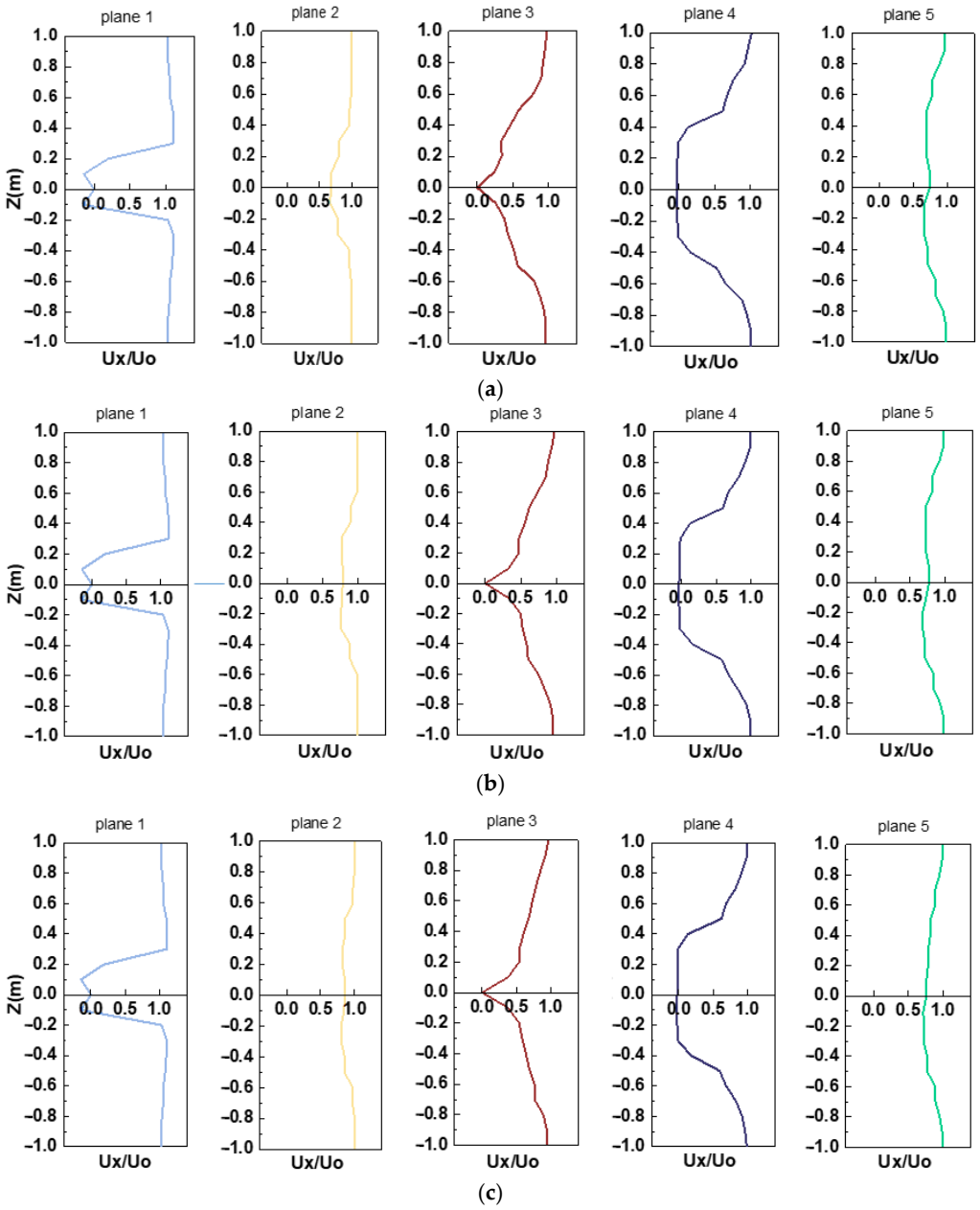

Figure 13. Dimensionless velocity profiles at various vertical cross sections for the fully constrained system at towing distances of (**a**) 5 m, (**b**) 10 m, and (**c**) 15 m.

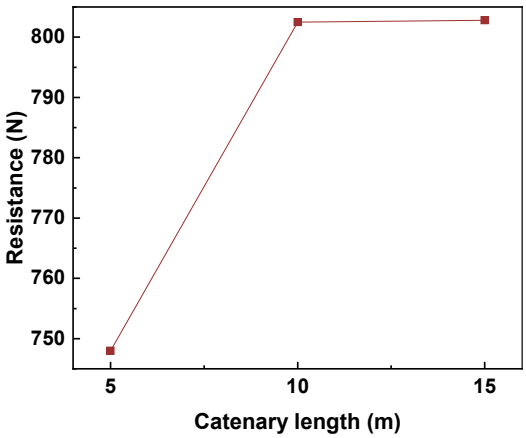

Figure 14. Hydrodynamic drag force of the secondary towed body at different separation distances under fully constrained conditions.

The locally magnified surface pressure distribution of the primary and secondary towed bodies is depicted in Figure 15, while the overall surface pressure distribution of the fully constrained towing system is shown in Figure 16. The pressure distribution follows the Bernoulli principle. As the bodies advance, the bow directly impacts the water, causing a sharp decrease in fluid velocity and creating a high-pressure stagnation point at the bow. When the fluid flows around the curved bow of the secondary towed body, its velocity increases rapidly, generating a pronounced negative pressure at the junction between the bow and the parallel midbody. The flow field near the midbody primarily exhibits simple advection with negligible hydrodynamic pressure effects. Comparing the cases at different distances reveals that the low-velocity wake region generated by the primary body exerts a stronger influence at shorter towing distances. Consequently, the fluid velocity near the bow is reduced, resulting in lower dynamic pressure. As the distance increases, the wake dissipates, causing a slight increase in inflow velocity and greater hydrodynamic pressure at the bow. Regardless of the towing distance, the hydrodynamic pressure distribution on the secondary body remains symmetric about its longitudinal axis.

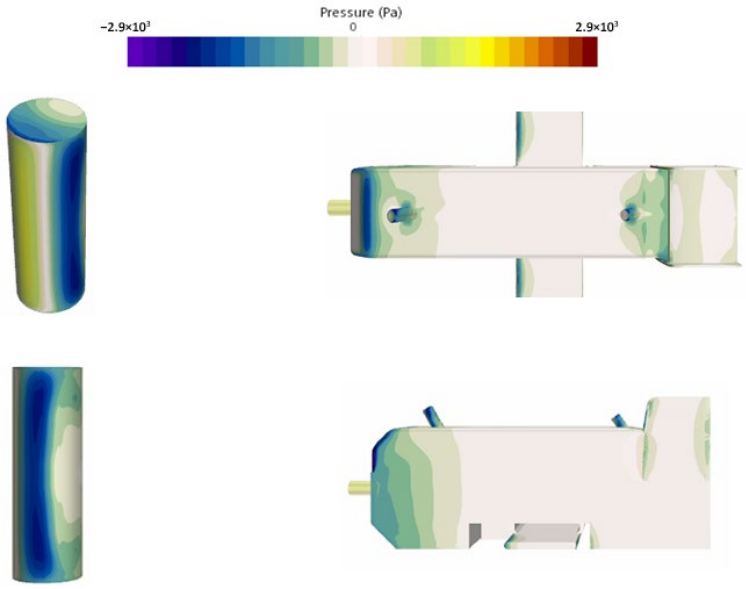

Figure 15. Locally magnified surface pressure distribution of the primary and secondary towed bodies.

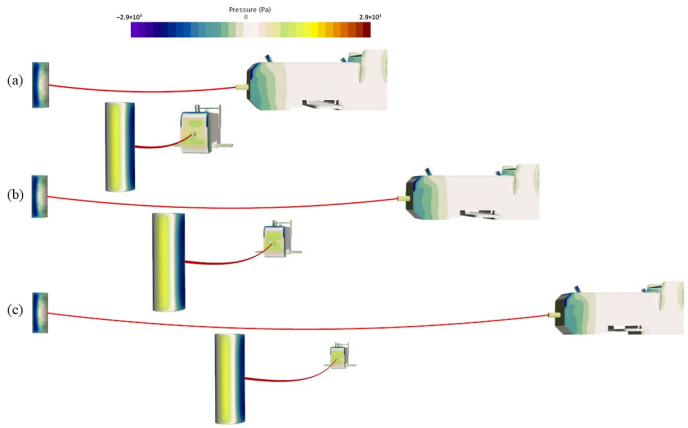

Figure 16. Overall surface pressure distribution of the fully constrained towing system at separation distances of (**a**) 5 m, (**b**) 10 m, and (**c**) 15 m.

3.2. Linearly Constrained Conditions

Under linearly constrained conditions, the secondary towed body is permitted to translate only along the longitudinal axis, while all other degrees of freedom remain fixed. This setup simulates the surge motion response of the system, allowing the cable tension to vary and the secondary towed body to oscillate forward and backward. Simulations were conducted in an infinite-depth environment with a towing speed of 1.543 m/s.

Figure 17 illustrates the dimensionless axial velocity contours on the vertical symmetry plane under linearly constrained conditions. As water flows around the system, low-velocity regions form at both the bow and stern of the towed bodies, while high-velocity regions appear on both sides of the primary towed body. As the towing distance increases, the momentum exchange intensifies, causing the low-velocity zone in the wake to dissipate gradually. Consequently, the influence of the wake generated by the primary body on the downstream secondary body becomes minimal. Under infinite-depth conditions, the low-velocity regions exhibit near symmetry. Data extracted from the designated vertical planes are presented in Figure 18, confirming that the wake velocity progressively increases with distance and the wake field behind the secondary body gradually approaches approximate symmetry.

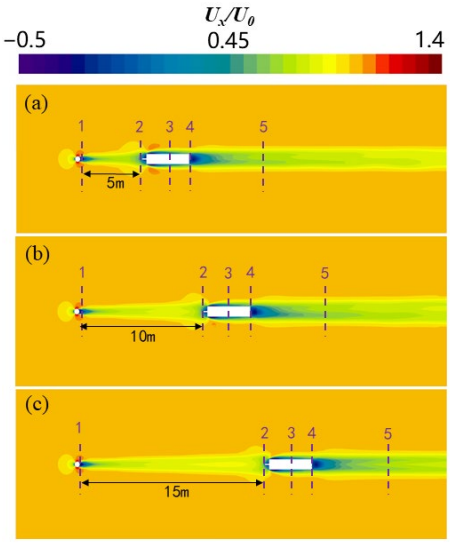

Figure 17. Dimensionless axial velocity contours on the vertical symmetry plane under linearly constrained conditions at separation distances of (**a**) 5 m, (**b**) 10 m, and (**c**) 15 m.

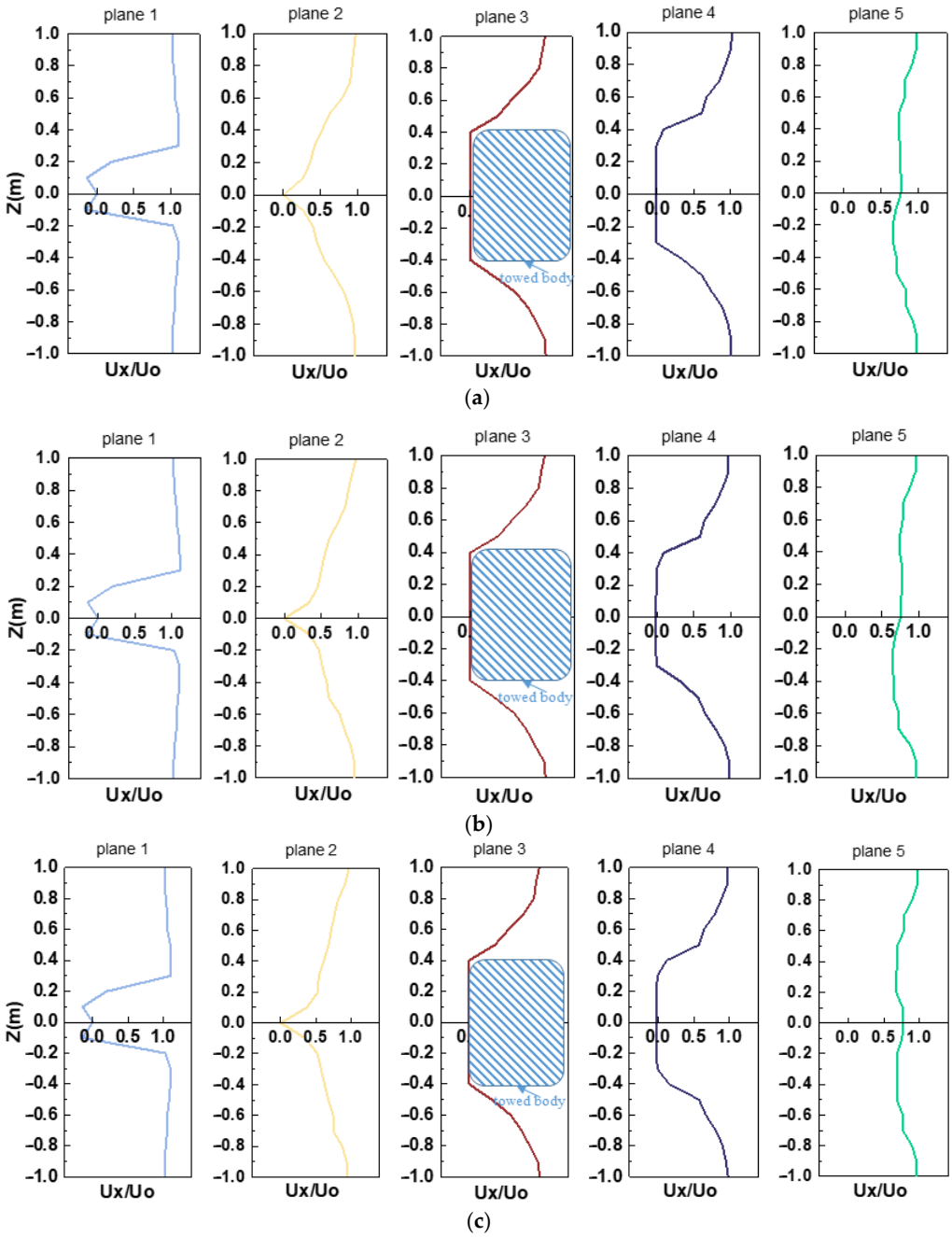

Figure 18. Dimensionless velocity profiles at designated vertical planes under linearly constrained conditions at separation distances of (**a**) 5 m, (**b**) 10 m, and (**c**) 15 m.

In the dynamic response analysis, the secondary towed body is considered to have returned to a stable state when the oscillation displacement is less than 0.01 m. Figure 19 shows the time history of the longitudinal displacement of the secondary towed body under linearly constrained conditions. The system reaches a steady state after approximately 35 s. The motion is characterized by damped oscillations, indicating that the hydrodynamic damping effectively dissipates the initial perturbation energy. To quantitatively assess this stability, dynamic metrics were extracted from the displacement time-history data in Figure 19. Following the initial transient peak of approximately 0.33 m at t ≈ 1.3 s, the surge motion exhibits a dominant damped oscillation frequency of approximately 0.21 Hz (corresponding to an average period of about 4.8 s), with the peak-to-trough oscillation amplitude decaying below the 0.01 m stability threshold after 35 s to reach a steady offset

of approximately 0.075 m. The faster decay of oscillation observed at longer separations can be attributed to two coupled effects: the secondary body is exposed to a weaker and more recovered wake disturbance, and the longer cable provides greater system compliance. Furthermore, the extended catenary cable acts as a mechanical low-pass filter; it decreases the overall structural stiffness, thereby shifting the natural frequency of the coupled system away from the dominant vortex-shedding frequency of the primary wake, which accelerates the dissipation of high-frequency oscillatory energy.

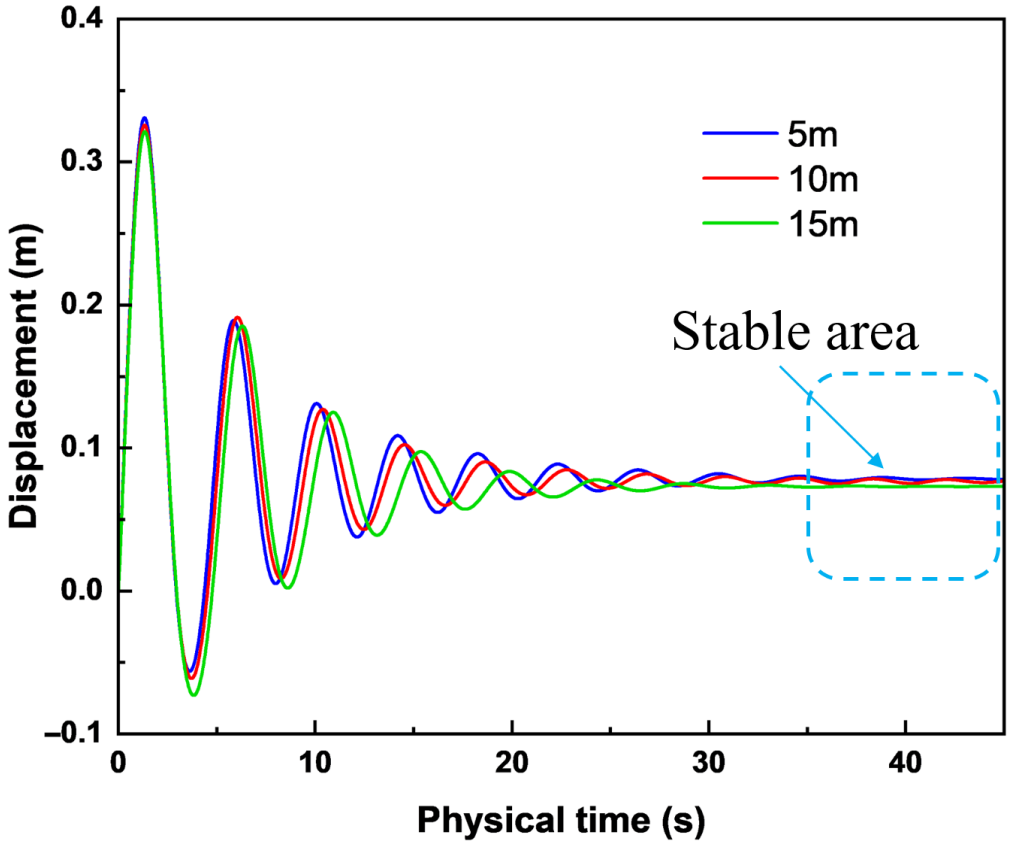

Figure 19. The displacement of towed body along the *x*-axis.

Figure 20 displays the hydrodynamic drag force of the secondary towed body under linearly constrained conditions. A direct comparison with the fully constrained condition reveals that while the baseline drag values are mathematically similar, the release of the longitudinal degree of freedom entirely transforms the static drag into a dynamically fluctuating load. During the towing process, the flow field surrounding the secondary body is influenced by the wake of the primary body, resulting in fluctuations in the drag force. Furthermore, the average drag acting on the secondary body increases from 771.79 N at a distance of 5 m to 785.56 N at a distance of 15 m. The lowest drag occurs at a towing distance of 5 m because the flow velocity at the bow of the secondary body is minimal within the strong wake shadow. The fluctuations in drag are directly attributed to the surge motion allowed by the linear control constraints. This oscillatory motion modifies the relative velocity distribution between the body and the surrounding fluid, leading to continuous variations in the drag force.

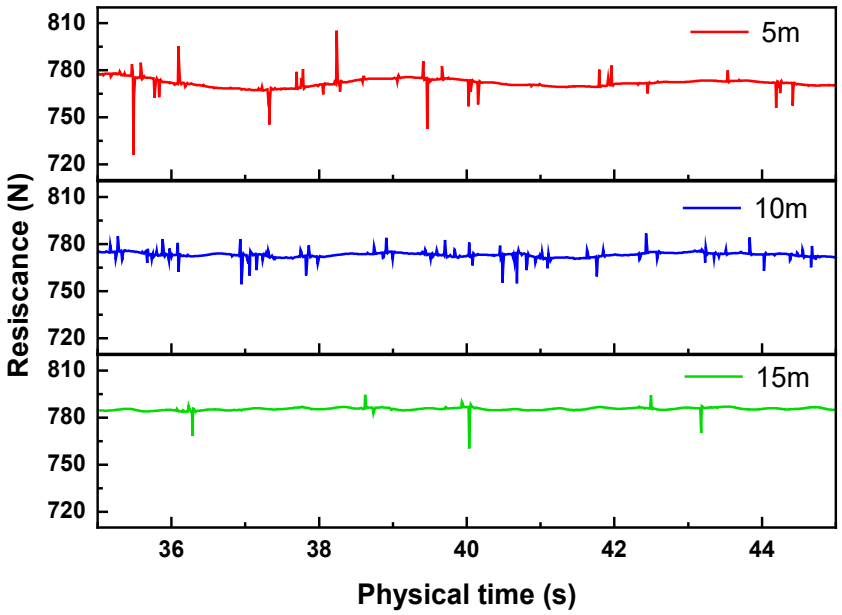

Figure 20. Time history of the hydrodynamic resistance of the secondary towed body under linearly constrained conditions at separation distances of 5 m, 10 m, and 15 m.

The cable tension time history at different towing distances under linearly constrained conditions is depicted in Figure 21, and an enlarged view of the stabilization region is shown in Figure 22. During the initial stage of motion, the secondary towed body is strongly influenced by the wake of the primary body, resulting in large-amplitude oscillations and corresponding fluctuations in cable tension. As the simulation progresses, the secondary body stabilizes, and the cable tension begins to exhibit regular periodic fluctuations. The results indicate that the average cable tension increases from 771.24 N at 5 m to 785.59 N at 15 m. This moderate increase should be interpreted as an auxiliary indicator of the changing load state rather than as an independent principal finding. Physically, it reflects the recovery of the local inflow momentum and the reduction in wake shielding as the separation distance increases. The linearly constrained results therefore provide supporting evidence for the coupled relation among wake recovery, drag fluctuation, and cable tension response. From a physical mechanism perspective, the dynamic behavior observed under linearly constrained conditions is governed by the strict coaxial alignment between the secondary body and the centerline of the upstream wake ($\Delta Z = 0$). Because the secondary body cannot migrate vertically out of the wake shadow, it remains continuously submerged within the central velocity-deficit core across all three separation distances. Consequently, as the relaxed cable length increases from 5 m to 15 m, the mean cable tension increases by only 14.35 N (or 1.86%, from 771.24 N at 5 m to 785.59 N at 15 m), which corresponds to stable longitudinal equilibrium positions of 5.7888 m, 10.7858 m, and 15.7751 m, respectively. This slight tension increment confirms that the coaxial wake shielding effect remains substantial along the centerline, preventing the abrupt load surge that would occur if the body entered the undisturbed mainstream. Furthermore, the faster attenuation of initial transient oscillations at larger separations (reaching quasi-steady equilibrium within approximately 35 s) stems from two synergistic physical mechanisms: first, the dissipation of large-scale coherent vortices at L/D = 37.5 reduces the unsteady hydrodynamic excitation force; second, the partially recovered local inflow velocity at 15 m increases the velocity-dependent hydrodynamic drag damping during longitudinal surging, which combines with the enhanced geometric compliance of the longer catenary cable to dissipate perturbation energy more efficiently.

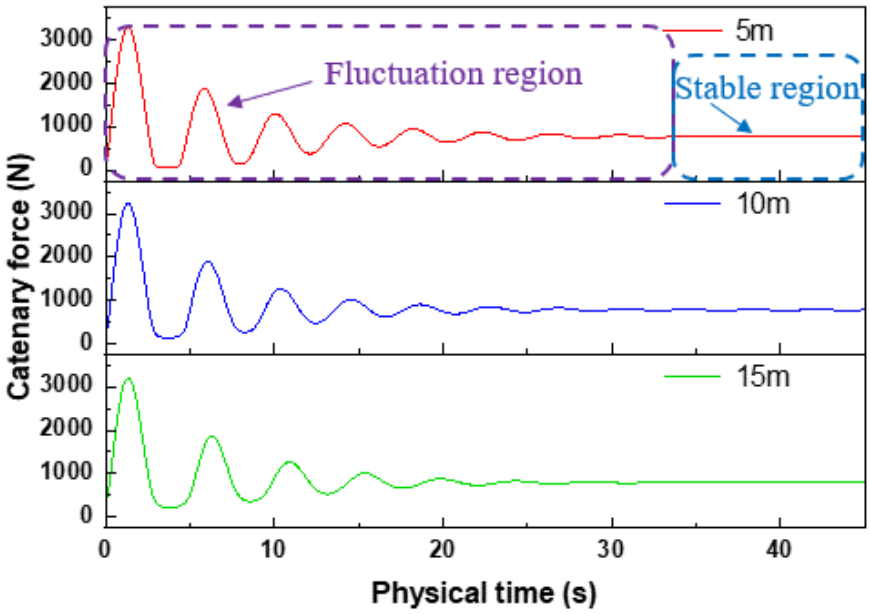

Figure 21. Cable tension time histories at different separation distances under linearly constrained conditions.

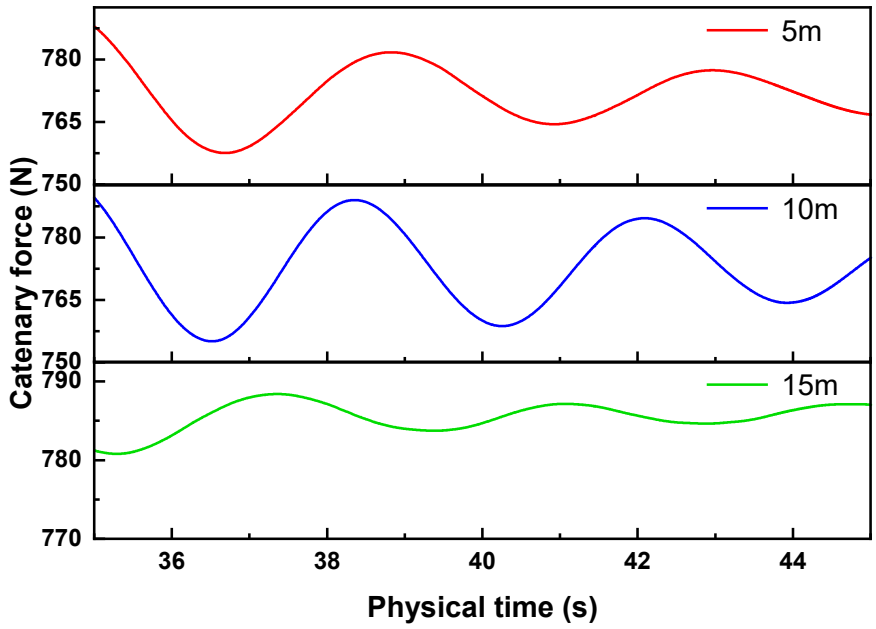

Figure 22. Local amplification of stabilization area of the different distances.

Figure 23 illustrates the surface pressure distribution of the towing system under linearly constrained conditions. When the towing distance is 5 m, the secondary body is positioned within the largest low-velocity wake region, resulting in relatively low hydrodynamic pressure. As the distance increases, the low-velocity wake region diminishes, and the flow velocity rises. The greater collision intensity between the bow of the secondary body and the incoming flow causes the hydrodynamic pressure acting on the bow to increase accordingly. The hydrodynamic pressure distribution remains symmetric about the central longitudinal axis throughout the process.

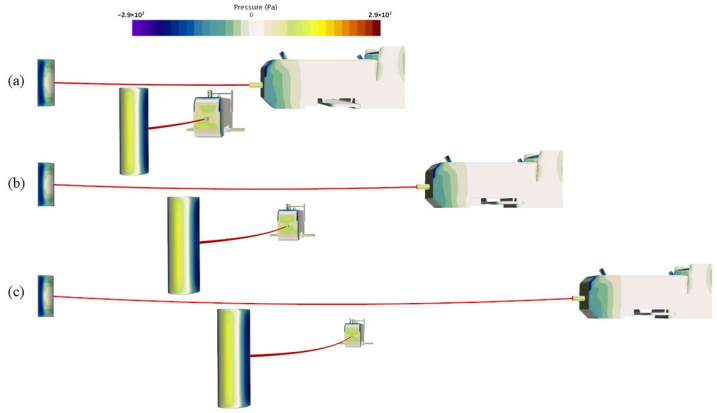

Figure 23. Surface pressure distribution of the towing system under linearly constrained conditions at separation distances of (**a**) 5 m, (**b**) 10 m, and (**c**) 15 m.

3.3. Planarly Constrained Conditions

Under planarly constrained conditions, the towing system is permitted to move along both the longitudinal and vertical directions. With adjustable cable tension, this two-degree-of-freedom setup allows the secondary towed body to translate and simulate coupled surge and heave motions. In this specific case, the released vertical motion indirectly reflects the combined dynamic action of buoyancy structural cable force and hydrodynamic lift even though the present paper does not list lift and trimming moment histories as explicit separate output variables.

Figure 24 illustrates the dimensionless axial velocity contours on the vertical plane under planarly constrained conditions at towing distances of 5 m, 10 m, and 15 m. When the vertical degree of freedom is released, the secondary body gradually moves away from the wake region of the primary body until it reaches a stable state. Due to the combined effects of its slight positive buoyancy, hydrodynamic lift, and cable tension, the secondary body rises to a stable vertical position at each towing distance. Additionally, flow separation caused by the vertical angle of attack creates a distinct low-velocity zone beneath the secondary body. Similarly to the linear control case, the proportion of the low-speed area at the bow decreases as the separation distance increases. Figure 25 confirms that the wake velocity of the primary body gradually increases with towing distance, and the wake behind the secondary body becomes increasingly symmetrical.

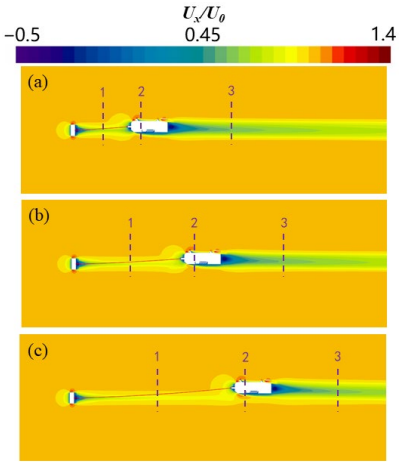

Figure 24. Figure 24. Dimensionless axial velocity U_x/U_0 in the x–y plane flow field at separation distances of (**a**) 5 m, (**b**) 10 m, and (**c**) 15 m.

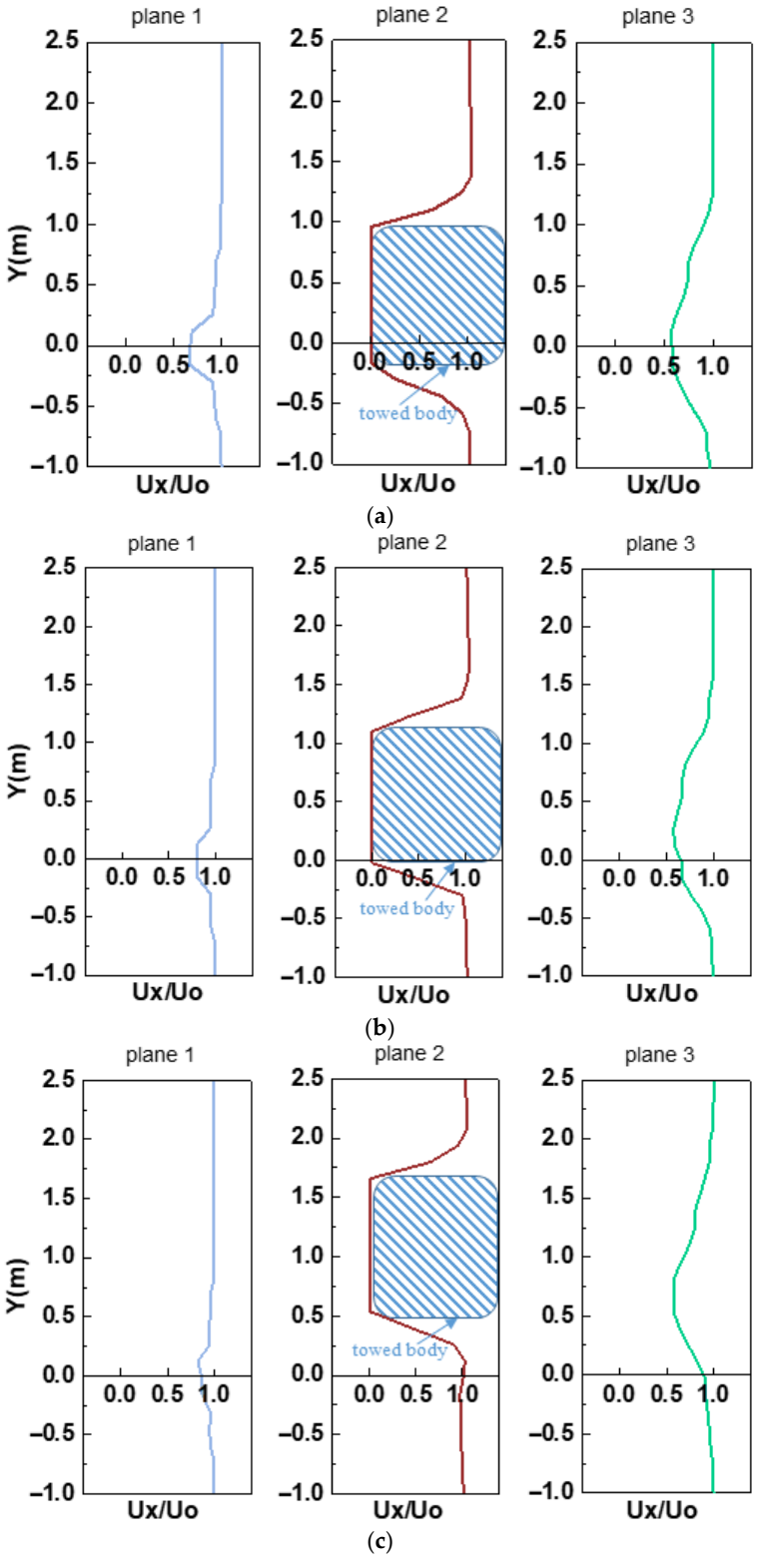

Figure 25. Dimensionless velocity profiles at designated vertical planes under planarly constrained conditions at separation distances of (**a**) 5 m, (**b**) 10 m, and (**c**) 15 m.

Figure 26 displays the vertical displacement time history of the secondary towed body at varying towing distances. The vertical displacement changes significantly with towing distance, reaching a stable displacement of 0.4465 m at the 5 m distance and increasing to 1.1451 m at the 15 m distance. The smallest displacement occurs at 5 m where the vertical component of the cable tension imposes a stronger restriction. The system attains a stable

state after 170 s, indicating that the system has reached a quasi-equilibrium condition. Quantitative metrics extracted from Figure 26 indicate that the vertical motion exhibits an overdamped response, reaching steady vertical equilibrium positions of 0.4465 m, 0.6302 m, and 1.1451 m after approximately 35 s, 65 s, and 160 s for the 5 m, 10 m, and 15 m separation distances, respectively. Within the quasi-equilibrium region ($t > 170$ s), the residual vertical oscillation amplitude is suppressed to less than 0.005 m across all cases, demonstrating strong vertical damping and reduced high-frequency jitter. This stability is crucial for maintaining the overall integrity and functionality of the towing system. The longitudinal displacement of the secondary towed body under planarly constrained conditions after 170 s is shown in Figure 27.

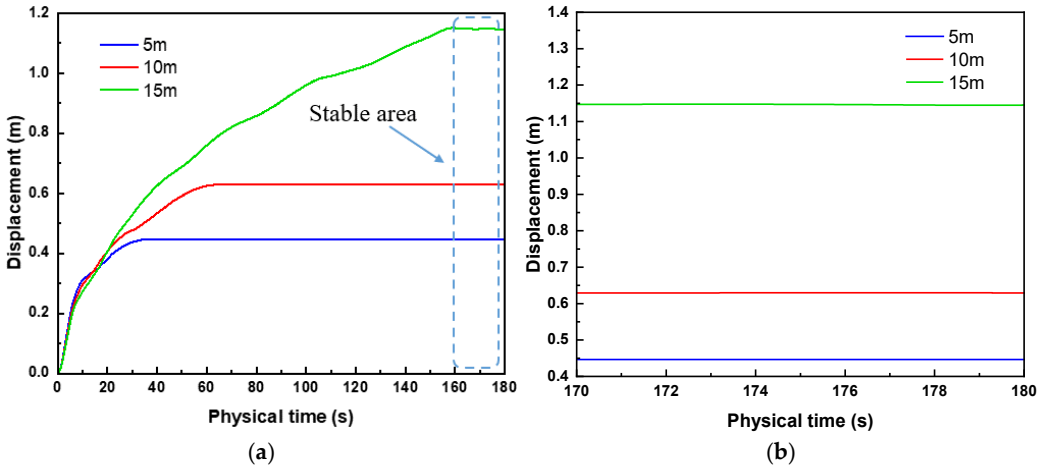

Figure 26. Displacement of the secondary body along the *y*-axis at different distances. (**a**) Vertical position change in towed body; (**b**) local amplification of stabilization area of vertical position change in towed body.

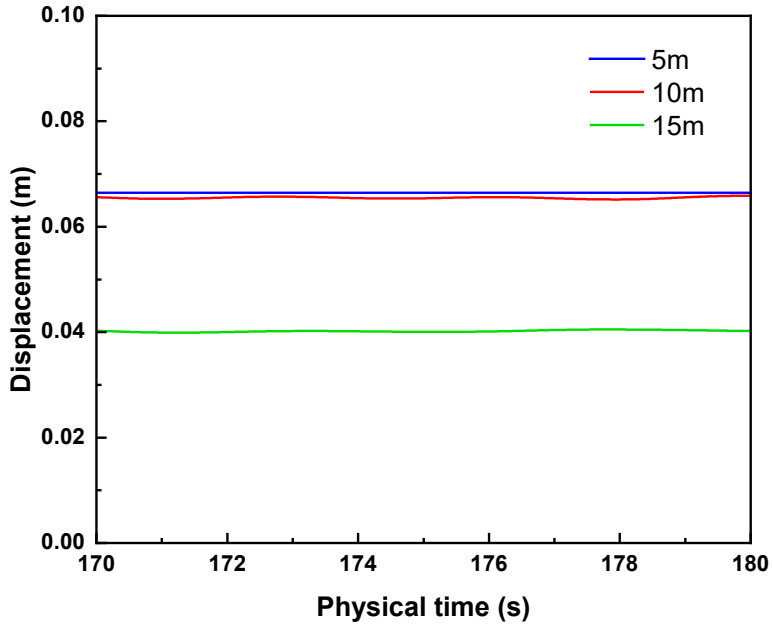

Figure 27. Displacement of the secondary body along the *x*-axis at different distances.

Figure 28 presents the hydrodynamic drag force of the secondary towed body under planarly constrained conditions. Similarly to the linear control case, the drag exhibits

periodic oscillations. However, the average drag under planar control is generally higher, increasing from 793.98 N at 5 m to 836.01 N at 15 m. Once the system stabilizes, the secondary body undergoes vertical displacement and no longer remains fully in the wake shadow of the primary body. Instead, the secondary body encounters the higher-velocity mainstream flow directly. Because the secondary body moves in both directions, its surrounding flow field is intermittently influenced by the wake of the primary body, which causes the secondary body to occasionally enter and exit the wake region, resulting in continuous drag fluctuations.

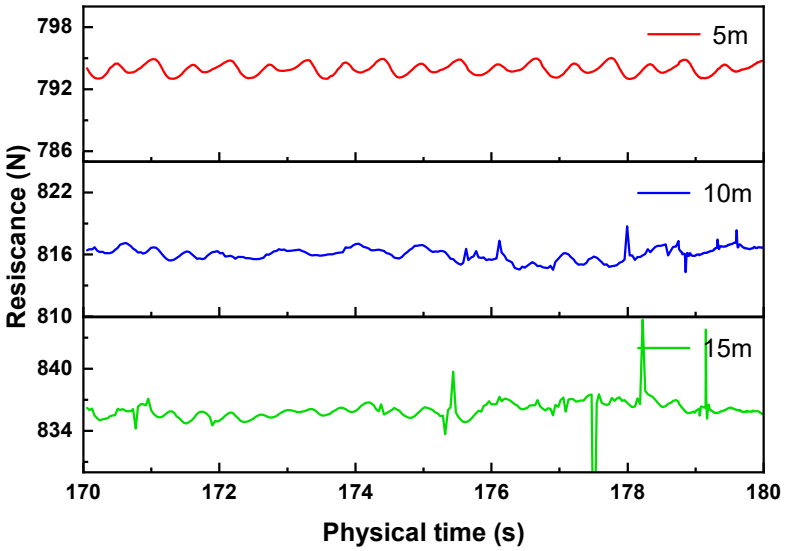

Figure 28. Time history of the hydrodynamic resistance of the secondary towed body under planarly constrained conditionsat separation distances of 5 m, 10 m, and 15 m.

The cable tension response at different separation distances under planarly constrained conditions is shown in Figure 29, with a magnified view of the stabilization region provided in Figure 30. After stabilization, the cable tension at each location exhibits periodic oscillations with relatively small amplitudes. When the cable tension reaches its peak, the displacement of the secondary body is also close to its local maximum. Physically, this in-phase relationship occurs because the axial tension in the quasi-static elastic catenary model is directly governed by the geometric elongation between the attachment points (k = 10,000 N/m); thus, the maximum downstream and vertical excursion of the secondary body directly induces peak elastic stretching in the cable. Furthermore, the average cable tension increases from 793.93 N at 5 m to 836.32 N at 15 m, representing an increment of 42.39 N (5.34%). By comparison, the corresponding tension increment under linearly constrained conditions is only 14.35 N (1.86%, from 771.24 N to 785.59 N). This quantitative difference demonstrates that releasing the vertical degree of freedom amplifies the sensitivity of cable tension to separation distance. Because the vertical elevation of the secondary body increases from 0.4465 m at 5 m to 1.1451 m at 15 m, the body progressively migrates out of the low-velocity wake shadow into the higher-momentum mainstream, requiring the cable tension to balance both the elevated longitudinal drag and the vertical force components. At greater distances, the frequency of reciprocating motion decreases and the motion range expands, suggesting that the dynamic response is governed by a trade-off between reduced wake disturbance, increased load levels, and enhanced compliance of the cable system.

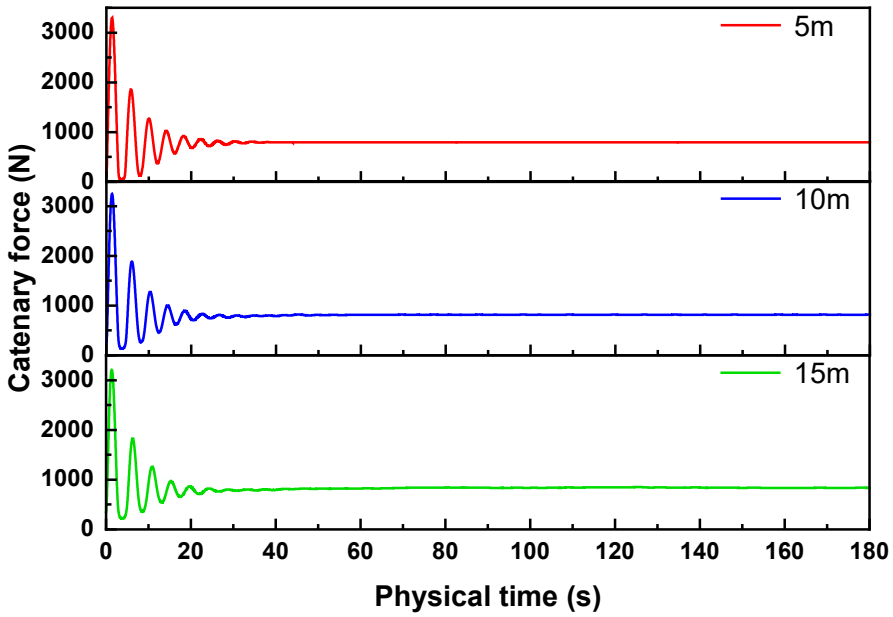

Figure 29. Cable tension response at different separation distances under planarly constrained conditions.

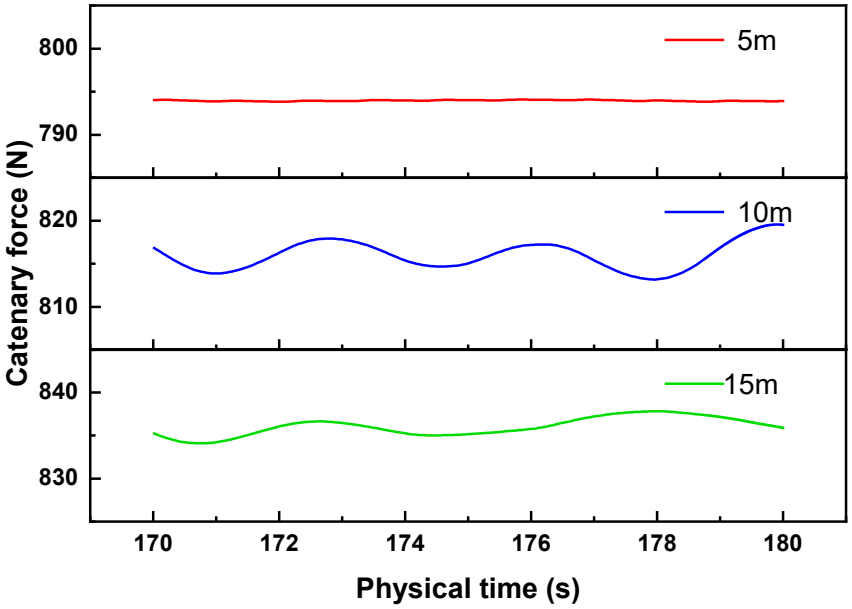

Figure 30. Magnified view of the cable tension stabilization region under planarly constrained conditions.

Figure 31 illustrates the surface pressure distribution of the towing system under planarly constrained conditions. When the system operates under planar control constraints, the surface pressure distribution on the secondary body displays a pattern fundamentally similar to that observed under linearly constrained conditions. Once the towing motion reaches a steady state, the system stabilizes at various vertical positions, and the cable tension becomes essentially constant. However, due to the release of the vertical degree of freedom, the secondary body at varying towing distances migrates away from the wake region generated by the primary body and stabilizes at progressively higher vertical elevations. At this stage, the bow of the secondary body directly encounters the undisturbed mainstream flow. The fluid velocity in front of the bow decreases sharply upon impact, creating an area

of extremely high hydrodynamic pressure at the stagnation point. As the flow navigates around the curved surfaces of the bow and stern tips of the secondary body, the local velocity accelerates rapidly, which consequently generates significant negative pressure zones along both sides of the bow. In contrast, the fluid motion near the parallel midbody can be characterized as simple advection, resulting in almost negligible hydrodynamic pressure variations along this section.

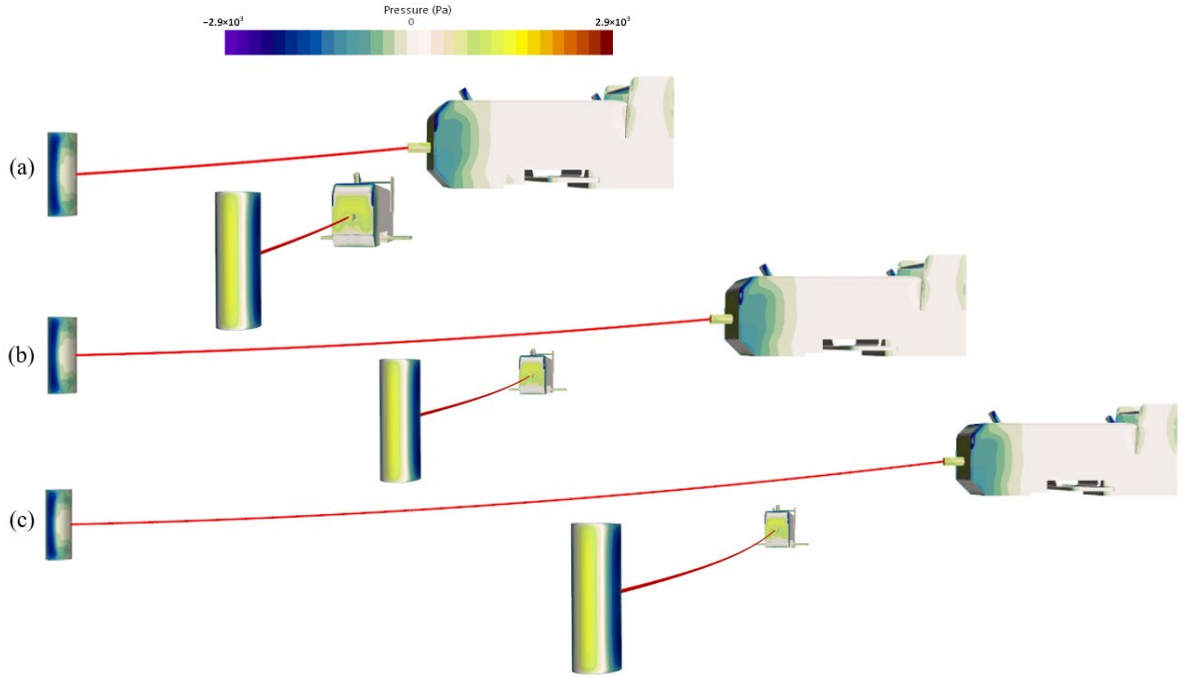

Figure 31. Surface pressure distribution of the towing system under planarly constrained conditions at separation distances of (a) 5 m, (b) 10 m, and (c) 15 m.

3.4. Comprehensive Comparative Analysis

To systematically illustrate the direct impact of releasing spatial degrees of freedom, comprehensive comparisons of the key hydrodynamic parameters are formally presented. Figure 32 compares the average hydrodynamic drag force on the secondary towed body across the three constraint conditions. A comprehensive analysis reveals a clear physical hierarchy in the drag magnitude where the planarly constrained system consistently experiences the highest average drag at all tested towing distances. Specifically, the average drag under planar control increases to 836.01 N at 15 m which is notably higher than the maximum average drag of 785.56 N observed in the linearly constrained case. Furthermore, Figure 33 compares the mean cable tension solely between the two dynamic configurations. The planar configuration reliably yields higher overall mean tension values reaching 836.32 N at 15 m compared to the 785.59 N recorded under linear constraints. This significant increase occurs primarily because the cable in the planar two-degrees-of-freedom setup must physically balance not only the enhanced longitudinal drag but also the vertical hydrodynamic lift and upward buoyancy components.

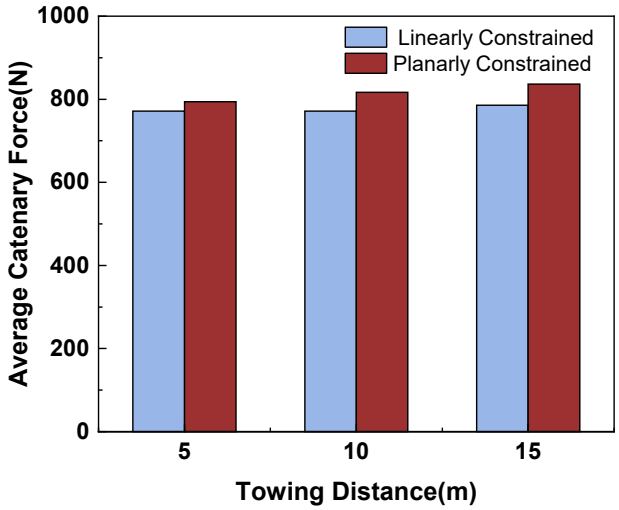

Figure 32. Comparison of the average hydrodynamic drag force on the secondary towed body across the three constraint conditions at various separation distances.

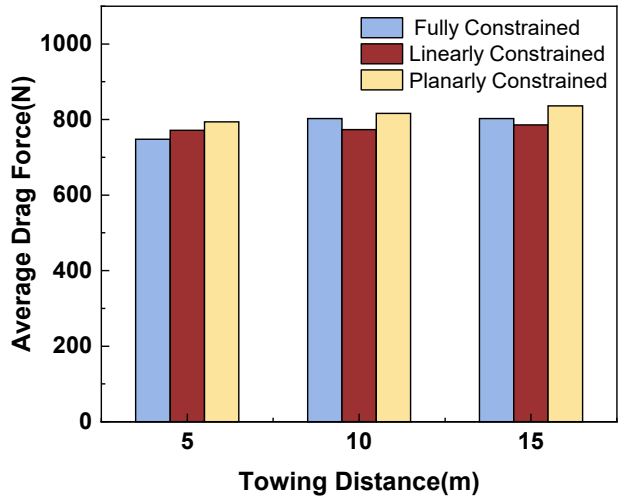

Figure 33. Comparison of the mean cable tension between the linearly and planarly constrained configurations at varying towing distances.

3.5. Model Limitations and Applicability

The present study has several limitations that should be considered when interpreting the results. First, the cylindrical primary body is a simplified depressor surrogate, and a detailed engineering depressor geometry may generate a different wake structure. Second, the infinite-depth computational domain excludes free-surface wave-making resistance and boundary layer effects from the seabed, making the conclusions most applicable to idealized mid-water conditions. Third, to focus strictly on body-to-body interference, direct hydrodynamic forces acting on the cable and complex ocean-current disturbances were neglected. Fourth, the three constraint cases are idealized boundary cases used for mechanism identification and do not represent the complete unconstrained six-degree-of-freedom motion (including rotational dynamics such as roll, pitch, and yaw) of a field-deployed two-stage towing system. Fifth, the present parametric matrix considers one representative towing speed and three separation distances; therefore, the distance at which the secondary body approaches an undisturbed-flow response cannot be generalized without additional simulations over body scales, speeds, depths, and cable properties.

Finally, while the RANS-based Realizable k-ε model captures mean loads effectively, future studies should employ scale-resolving CFD techniques, such as large-eddy simulation (LES), to resolve fine-scale coherent vortices and provide explicit histories of lift forces and trimming moments. Rigorous physical model-test validations for the specific two-stage configuration are also essential to verify these coupled hydrodynamic responses comprehensively.

4. Conclusions

This study investigated the hydrodynamic resistance characteristics and coupled motion responses of a two stage deep towing system using computational fluid dynamics. Numerical simulations were successfully conducted under infinite depth conditions to evaluate the system performance across fully constrained, linearly constrained, and planarly constrained configurations. It must be reiterated that these progressive constraint setups are idealized mechanism-study cases formulated to isolate specific coupling effects, and do not fully reflect unconstrained, real-world six-degree-of-freedom deep-towing operations. This rigorous research yields several fundamental insights into the dynamic fluid structure interaction of the towing system.

The baseline analysis under fully constrained conditions reveals that the wake generated by the primary towed body exhibits a symmetrical structure along the central longitudinal axis. The hydrodynamic drag exerted on the secondary towed body is heavily governed by the wake-shielding effect. At a short separation distance of 5 m ($L/D = 12.5$), the secondary body resides entirely within the low-velocity near-wake core, experiencing reduced drag accompanied by intense turbulent fluctuations. As the separation distance increases to 10 m ($L/D = 25$) and 15 m ($L/D = 37.5$), the dissipation of the primary wake and the nonlinear recovery of the local inflow velocity cause the mean drag of the secondary body to increase progressively, with a reduced increment between 10 m and 15 m. Within the three tested distances, these results demonstrate a gradual transition toward a less-disturbed flow regime, whereas determining the exact critical spacing required to fully recover the undisturbed isolated-body resistance warrants future parametric investigations over wider separation ranges.

Transitioning to the linearly constrained conditions, the release of the longitudinal degree of freedom induces damped surge oscillations. Once the system reaches a quasi-equilibrium state, the secondary body undergoes periodic reciprocating motion driven by the dynamic interaction between the hydrodynamic drag and the connecting cable tension. The numerical results indicate that a shorter towing distance places the secondary body in a highly disturbed wake region, resulting in lower mean cable tension but significantly higher oscillation frequencies. Conversely, increasing the separation distance effectively enhances the longitudinal stability of the system.

Further expanding the kinematic freedom under planarly constrained conditions, the coupled surge and heave motions allow the secondary body to migrate vertically to achieve force equilibrium. As the towing distance increases, the secondary body stabilizes at progressively higher vertical positions and partially exits the wake region of the primary body. The altered angle of attack and the direct exposure to higher-velocity flow lead to increased hydrodynamic drag and mean cable tension. However, the extended cable length reduces the frequency of the reciprocating motion and provides a significantly larger buffer range, thereby improving the overall motion stability of the towing system in complex underwater environments.

While the present study successfully isolates the fundamental mechanisms of wake shielding and constrained stability, future work will focus on integrating fully unconstrained six-degree-of-freedom motions, realistic wave-induced disturbances, and physical model

tests to further bridge the gap between idealized numerical models and complex deep-sea operations.

Author Contributions: Conceptualization, K.W. and B.L.; methodology, K.W. and B.L.; software, B.L.; validation, B.L. and Q.Z.; formal analysis, B.L. and C.Z.; investigation, B.L., Q.Z. and C.Z.; resources, K.W.; data curation, B.L.; writing—original draft preparation, B.L.; writing—review and editing, K.W. and C.C.; visualization, B.L. and Q.Z.; supervision, K.W.; project administration, K.W.; funding acquisition, K.W. All authors have read and agreed to the published version of the manuscript.

Funding: This research was funded by the National Key Research and Development Program of China, grant number 2023YFC2808704, and the National Natural Science Foundation of China, grant number 52376157.

Institutional Review Board Statement: Not applicable.

Informed Consent Statement: Not applicable.

Data Availability Statement: The original contributions presented in this study are included in the article. Further inquiries can be directed to the corresponding author.

Acknowledgments: The authors gratefully acknowledge research support from the National Key Research and Development Program of China (No. 2023YFC2808704), National Natural Science Foundation of China (No. 52376157).

Conflicts of Interest: The authors declare no conflicts of interest.

Nomenclature

A	Reference area of the secondary towed body (m^2)	I	Moment of inertia
C_D	Hydrodynamic drag coefficient	u_i	Velocity component in the i direction(m/s)
C_L	Hydrodynamic lift coefficient	x,y,z	Cartesian coordinates (m)
D	Characteristic length/diameter of the towed body (m)	**Greek symbols**	
d	Distance between the primary and secondary towed bodies (m)	ε	Turbulent dissipation rate(m^2/s^3)
F_D	Hydrodynamic drag force (N)	μ	Viscosity (Pa·s)
F_L	Hydrodynamic lift force (N)	ν	Kinetic viscosity (m^2/s)
g	Gravitational acceleration(m/s^2)	ρ	Density (kg/m^3)
m	Mass of the towed body (kg)	τ	Shear stress (Pa)
p	Static pressure (Pa)	k	Turbulent kinetic energy
F_T	Tension in the towing cable (N)	**Subscripts**	
U	Flow velocity magnitude(m/s)	D	Drag
Re	Reynolds number	L	Lift
S	Area (m^2)	i,j	Coordinate directions
t	Time (s)	b	Buoyancy contribution

References

1. Hsu, H.H.; Lin, L.F.; Liu, C.S.; Chang, J.H.; Liao, W.Z.; Chen, T.T.; Chao, K.H.; Lin, S.L.; Hsieh, H.S.; Chen, S.C. Pseudo-3D seismic imaging of Geolin Mounds hydrothermal field in the Southern Okinawa trough offshore NE Taiwan. *Terr. Atmos. Ocean Sci.* **2019**, *30*, 705–716. [CrossRef]
2. Hong, L.; Wang, X.; Zhang, D.S. CFD-based hydrodynamic performance investigation of autonomous underwater vehicles: A survey. *Ocean Eng.* **2024**, *305*, 117911. [CrossRef]
3. Wang, Y.; Cheng, Z.; Yin, B.; Liu, B.; Wang, K. Simulation of special-shaped graded particulate hydraulic transport in deep-sea mining scenarios. *Powder Technol.* **2024**, *448*, 120344. [CrossRef]
4. Cheng, Z.; Wang, K.; Yin, B.; Wang, Y.Y. Particle transport mechanisms in an ocean-disturbed curved lift pipeline for deep-sea mining. *Chem. Eng. Sci.* **2025**, *321*, 122849. [CrossRef]
5. Cheng, Z.; Wang, K.; Wang, Y.Y. Dynamic mixing pipe under deep-sea current disturbance. In Proceedings of the ASME 2025 44th International Conference on Ocean, Offshore and Arctic Engineering (OMAE2025), Vancouver, BC, Canada, 22–27 June 2025.

6. Delmer, T.N.; Stephens, T.C.; Coe, J.M. Numerical simulation of towed cables. *Ocean Eng.* **1983**, *10*, 119–132. [CrossRef]
7. Buckham, B.; Nahon, M.; Seto, M.; Zhao, X.; Lambert, C. Dynamics and control of a towed underwater vehicle system, part I: Model development. *Ocean Eng.* **2003**, *30*, 453–470. [CrossRef]
8. Bettles, R.W.; Chapman, D.A. The experimental verification of a towed body and cable dynamic response theory. *Ocean Eng.* **1985**, *12*, 453–469. [CrossRef]
9. Mansoorzadeh, S.; Javanmard, E. An investigation of free surface effects on drag and lift coefficients of an autonomous underwater vehicle (UUV) using computational and experimental fluid dynamics methods. *J. Fluid Struct.* **2014**, *51*, 161–171. [CrossRef]
10. Zoysa, A.P.K.D. Steady-state analysis of undersea cables. *Ocean Eng.* **1978**, *5*, 209–223. [CrossRef]
11. Friswell, M.I. Steady-state analysis of underwater cables. *J. Waterw. Port. Coast. Ocean Eng.* **1995**, *121*, 98–104. [CrossRef]
12. Guan, G.; Zhang, X.; Wang, Y.; Yang, Q. Analytical and numerical study on underwater towing cable dynamics under different flow velocities based on experimental corrections. *Appl. Ocean Res.* **2021**, *114*, 102768. [CrossRef]
13. Wu, J.; Chwang, A.T. A hydrodynamic model of a two-part underwater towed system. *Ocean Eng.* **2000**, *27*, 472–495. [CrossRef]
14. Wu, J.; Chwang, A.T. Investigation on a two-part underwater maneuverable towed system. *Ocean Eng.* **2001**, *28*, 1079–1096. [CrossRef]
15. Yang, X.; Wu, J.; Xu, S. Dynamic analysis of underwater towed system under undulating motion mode of towed vehicle. *Appl. Ocean Res.* **2022**, *121*, 103083. [CrossRef]
16. Yang, X.; Wu, J.; Xu, S. Study on dynamic response of underwater towed system in ship propeller wakes using a new hydrodynamic model. *Ocean Eng.* **2022**, *265*, 112599. [CrossRef]
17. Wu, J.; Yang, X.; Xu, S.; Han, X. Numerical investigation on underwater towed system dynamics using a novel hydrodynamic model. *Ocean Eng.* **2022**, *247*, 110632. [CrossRef]
18. Tran, T.T.; Kim, D.H. The coupled dynamic response computation for a semisubmersible platform of floating offshore wind turbine. *J. Wind Eng. Ind. Aerod.* **2015**, *147*, 104–119. [CrossRef]
19. Song, K.; Guo, C.; Wang, C.; Sun, C.; Li, P.; Wang, W. Numerical analysis of the effects of stern flaps on ship resistance and propulsion performance. *Ocean Eng.* **2019**, *193*, 106621. [CrossRef]
20. Foroushani, J.A.; Sabzpooshani, M. Determination of hydrodynamic derivatives of an ocean vehicle using CFD analyses of synthetic standard dynamic tests. *Appl. Ocean Res.* **2021**, *108*, 102539. [CrossRef]
21. Ku, G.; Cho, J.; Cheong, C.; Seol, H. Numerical investigation of tip-vortex cavitation noise of submarine propellers using hybrid computational hydro-acoustic approach. *Ocean Eng.* **2021**, *238*, 109693. [CrossRef]
22. Liu, H.L.; Huang, T.T. *Summary of DARPA SUBOFF Experimental Program Data*; Technical Report; Naval Surface Warfare Center, Carderock Division (NEWCCD): West Bethesda, MD, USA, 1998; Available online: https://www.readcube.com/articles/10.21236/ada359226 (accessed on 1 November 2023).

Disclaimer/Publisher's Note: The statements, opinions and data contained in all publications are solely those of the individual author(s) and contributor(s) and not of MDPI and/or the editor(s). MDPI and/or the editor(s) disclaim responsibility for any injury to people or property resulting from any ideas, methods, instructions or products referred to in the content.